3-24-2006

Tracking Fluid Flow in a Spinning Disk Reactor

Valentina N. Korzhova
University of South Florida

Tracking Fluid Flow in a Spinning Disk Reactor

by

Valentina N. Korzhova

A thesis submitted in partial fulfillment
of the requirements for the degree of
Master of Science in Computer Science
Department of Computer Science and Engineering
College of Engineering
University of South Florida

Major Professor: Dmitry B. Goldgof, Ph.D.
Rangachar Kasturi, Ph.D.
Sudeep Sarkar, Ph.D.

Date of Approval:
March 24, 2006

Keywords: inclination angle, mathematical modeling, spiral wave, velocity components, wavelength

DEDICATION

This thesis is dedicated, especially, to

my parents

and, also, to

my husband, son, and daughter for

their love, support, guidance, and understanding.

ACKNOWLEDGEMENTS

I would like to thank Dr. Dmitry Goldgof for giving me the opportunity to work with him and the invaluable academic guidance and hours that he dedicated in the doing of this thesis. I also thank Dr. Rangachar Kasturi and Dr. Sudeep Sarkar for the time they took to review this thesis and their helpful comments. I am grateful also to Dr. Sisoev for useful discussions and help. I would like to thank my family and all of my friends who gave me inspiration, support, and comfort throughout this tough road.

TABLE OF CONTENTS

LIST OF TABLES

LIST OF FIGURES

TRACKING FLUID FLOW IN A SPINNING DISK REACTOR

Valentina N. Korzhova

ABSTRACT

The flow of a liquid film over a rapidly rotating horizontal disk has many applications in medical, industrial, and engineering fields. A specific example is the heat and mass transfer processes between expanded liquid and surrounded dense gas. Different wave regimes of a liquid film depend on a flow conditions such as the properties of a liquid, its initial speed, parameters of environment, etc. Therefore, experimental investigation of the film flow over a spinning disk is needed to both validate theoretical predictions and establish methods for fluid flow monitoring.

This thesis presents novel video-based algorithms for detection and tracking wave structural data of the liquid film flowing over a spinning disk reactor. The algorithms are based on the spiral model of wave and the quasi-optimal method for estimation of a wave velocity as ill-posed problem. Their performance is compared with results predicted by the fluid dynamics based on the Navier-Stokes equations in the case of thin film.

Using experimental video data, the developed models and algorithms allow investigators to estimate the characteristics of wave regimes such as wavelengths, inclination angles, and the radial and azimuthal velocity components of the fluid. The accuracy of estimated characteristics was analyzed. It was shown that average distance between consecutive two waves, their spiral shapes, and the radial velocities of waves confirm the theoretical results and predictions. In particular, computed wavelength is within 1% and a change of the inclination angles is within 2% of the predicted values.

CHAPTER 1

INTRODUCTION

1.1 Overview of the Related Work

The flow of a liquid film over a rapidly rotating horizontal disk has many applications in chemical, medical, engineering and bioengineering fields. Examples of important applications are processes of heat or mass transfer between expanded liquid and surrounded gas, blood oxygenation, and cooling devices. To intensify those processes, technological performance has to adjust hydrodynamic parameters of flow with relevant chemical kinetics. So, the controlled film flow is used. Controlling transport rates in the liquid film offers the possibility of the formation of different kind of waves. Since various regimes of film flow have strong influence on those processes, it is important to control the formation of the regimes.

The experimental investigations of flow over a spinning disk have attempted to measure local maximum or mean of a film thickness to obtain information about surface waves [2]. Various mechanical [6, 24], electrical [4, 29], and optical [19, 48] techniques were employed. The most promised was the optical method used to collect information about waves observed. In the respective experiments, a camera was placed above the disk and connected to a computer providing with video imaging hardware and software. To measure film thickness over a disk domain, calibration of mechanical and optical tools and estimation of absorption coefficient were used. All, mechanical, electrical, and optical techniques gave insufficient information for classifying wave regimes and selecting most efficient regime for specific technological applications.

Early experimental investigations [6, 11] provided some qualitative and quantitative understanding the effect of flow-rate and rotational speed on the flow characteristics for a given set of physical parameters. Experimental observations [2, 4, 19, 20, 22, 31, 42, 48] have demonstrated that at a small flow-rate, a smooth film is formed, and at a moderately higher

flow-rate, circumferential waves moving from the disk center to the disk periphery are formed. Further increasing flow rate leads to the appearance of spiral waves unwinding in the direction of rotation [20]. It is shown in [48] that the initially uniform film breaks down into well-defined spiral ripples, which then break down further into a confused assembly of wavelets. Circumferential and spiral waves were found to decay at large disk radii. Comparison those observed waves and their associated parameters with the waves belonging to the first family and second family of waves in falling films shows their similarity. The waves in falling films were studied experimentally in the classical work [17] and theoretically in [3, 5].

Theoretical explanation of experimental results has received increasing attention in recent published research. There are three main directions for theoretical investigations of a film flow over a rotating disk: calculation of waveless flow, analysis of its linear stability, and non-linear simulations of finite-amplitude waves. The waveless solutions, asymptotic and numerical, were investigated in [14, 28, 30]. These solutions generalize the Nusselt solution in series expansion in the powers of the Eckman number or the radius. Steady flow in the frame of the boundary layer approximation was considered in [10, 40]. The linear stability analysis was examined and performed using asymptotic methods [6, 27] and the full NavierStokes equation for finite Eckman numbers [38, 39].

In recent papers [21, 35, 36, 37] an evolution system of equations to model axis-symmetric finite-amplitude waves was derived and analyzed; this model was extended for non-axis-symmetric flows to explain the experimental results. Nevertheless, there are problems that could be treated by parallel application experimental and theoretical approaches: sensitivity of wave regimes to flow conditions and three-dimensional structures observed in experiments.

In the last decade, there has been significant work in image processing related to the motion analysis of non-rigid objects [8, 16]. In [16], the authors show that Finite Element Modeling shows promise for motion analysis of biological objects. Most of the works have concentrated on articulated and elastic motion [1, 13], but analysis of fluid-like motion was also attempted [8, 26, 49, 52].

Recently, work has begun in an effort to combine precise experimental setup, theoretical derivation, and basic image analysis techniques [43, 44, 48]. The equations constitute a set of physical constraints that are different [16] from those commonly used in the study of solid

motion, e.g., the rigidity constraint. For the fast fluid-like motion in the air, having turbulent character, detection of interface between fluid and air is important. A special so-called particle image velocimetry (PIV) technique was developed [23] to measure the kinematics of turbulent fluid flow in controlled laboratory experiments. Given a typical ensemble of PIV images, the aim is to calculate the instantaneous interface, including the instantaneous velocity on the surface of fluid and air contact, efficiently and with a reasonable degree of accuracy. Algorithms used are typically based on filter-like motion.

The 3D vectors of model variables describing fluid motion are varying in space. In practice, however, experimental data, obtained for a sequence of time instants, contain information that, generally speaking, differs from the model variables.

The purpose of this research is to develop a system of visual scanning, recording, and tracking of the film flow over a spinning disk with the intention to detect regimes of the fluid flow with regard to different conditions using a single camera system, to calculate fluid flow parameters and characteristics, and to compare them with the solutions of the relevant mathematical models. In this research, combination of direct visualization with image analysis software, utilizing results and methods of mathematical modeling is suggested.

1.2 Contributions of this Thesis

This thesis describes the following novel research contributions:

1. Unlike the majority of previous works, estimation of velocity components is given with estimates of the respective relative errors based on the so-called quasi-optimal method for the solution of ill-posed problems.

2. For practical realization of that quasi-optimal method, one needs to know estimates of the second and higher derivatives of the motion. The second derivatives can be estimated due to the Newton's law through the ratio of the respective forces to the mass. So, the contribution of this thesis is effective estimation of the second derivatives based on the model of spirals of waves with regard to three forces of the fluid flow over a spinning disc: centrifugal, friction over surface of the disc, and air resistance.

3. The third contribution is experimental estimation of wave inclinations, using the video image of radii as the function of azimuthal angle, which allows one to use arbitrary step along the angle under estimation of derivatives of radii over angles. On contrary, using experimental motion as the function of the time for estimation of wave inclinations may require too small time-step which cannot be realized in practice.

4. The novel model of spirals of waves and its numerical realization show rather good coincidence with the experimental spirals. So, the fourth contribution is a novel rather simple model (in comparison with the general model of Navier-Stokes), which can be useful for estimations of various parameters and characteristics of spiral waves.

1.3 Layout of the Thesis

Chapter 2 consists of description of the general theory of fluid flow based on the equations of Navier-Stokes, including the important particular case of the thin film flow. Besides the well-known results of various authors, especially Professor Sisoev, the chapter contains a novel equations of spirals of waves, which compared later with the respective experimental data and uses for the proper estimations of wave velocity components.

Chapter 3 describes experimental set up and camera calibration. Section 3.1 is devoted to data acquisition for the experimental disc reactor used in this study and to comparison of the data and reactor with the similar ones of the other authors and works [19, 42, 48]. Sections 3.2 and 3.3 describe the algorithm of camera calibration, and gives the analysis of its accuracy, which is used in Chapter 4 under estimation of errors of experimental velocity components and inclination angle.

Chapter 4 consists of description of experimental results and algorithms for estimates of parameters of wave spirals such as their velocity components, inclination angles, and wavelengths. It describes comparison of those results with the related results of theoretical models introduced in Chapter 2. It should be noted that the algorithms of this chapter are focused on automatic data processing starting from the initial video data and ending by the results of the analysis, including estimation of errors of numerical results. Qualitative and quantita-

tive comparison shows rather good coincidence (within 1-2%) of experimental and theoretical results.

CHAPTER 2

THEORY OF FLUID FLOW

2.1 General Case

This Chapter describes the mathematical models of fluid flow [9]. Consider an ideal inviscid fluid. The parameters of fluid mechanics are: the fluid density $\rho(x,t)$, the velocity vector field $u(x,t)$, and the pressure $p(x,t)$; $x \in R^d$ is the spatial coordinate in d-dimensional region of space. An infinitesimal element of the fluid of value δV located at position x at time t has mass $\delta m = \rho(x,t)\delta V$ and is moving with velocity $u(x,t)$ and momentum $\delta m u(x,t)$. The normal force directed into the infinitesimal volume across a face of area $n\delta a$ centered at x is $-n\rho(x,t)\delta a$, where n is the outward unit vector normal to the surface. The pressure is the magnitude of the force per unit area. These definitions are illustrated in Figure 2.1.

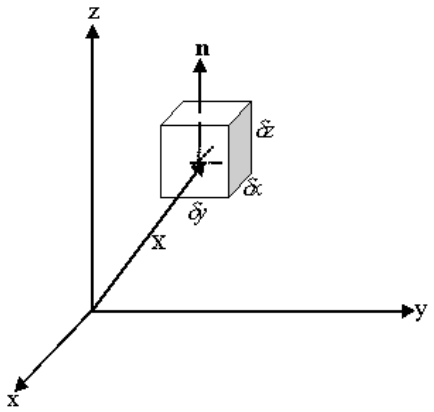

Figure 2.1 Fluid Element of Volume $\delta V = \delta x \delta y \delta z$ Located at Position X.

Recalling the definition of the convective derivative and the equation of the conservation of mass [9], the Euler's equations for an incompressible homogeneous fluid are:

$$\frac{\partial u}{\partial t} + u \cdot \nabla u = -\frac{1}{\rho}\nabla p,$$
$$\nabla \cdot u = 0,$$

where $\nabla = (\frac{\partial}{\partial x}, \frac{\partial}{\partial y}, \frac{\partial}{\partial z})$.

If an external force is applied to the fluid, then Euler's equations for an incompressible fluid become

$$\frac{\partial u}{\partial t} + u \cdot \nabla u + \frac{1}{\rho}\nabla p = \frac{1}{\rho} f(x,t), \quad \nabla \cdot u = 0,$$

where $f(x,t)$ is the applied force per unit volume. An incompressible fluid can be described with the Navier-Stokes equations that are four coupled nonlinear partial differential equations for four unknown functions (the three components of u and the pressure p):

$$\frac{\partial u}{\partial t} + u \cdot \nabla u + \frac{1}{\rho}\nabla p = \nu \Delta u + \frac{1}{\rho} f(x,t), \quad \nabla \cdot u = 0,$$

where ν is the kinematics' viscosity. The diffusion of momentum between neighboring elements of the fluid is a new ingredient in the incompressible Navier-Stokes equations comparing to the incompressible Euler equations. Also, there is the matter of boundary conditions [9].

Using the cylindrical system coordinates, the steady Navier-Stokes equations are:

$$u\frac{\partial u}{\partial r} + w\frac{\partial u}{\partial z} - \frac{v^2}{r} = -\frac{1}{\rho}\frac{\partial p}{\partial r} + \nu\left(\frac{\partial^2 u}{\partial z^2} + \frac{\partial^2 u}{\partial r^2} + \frac{1}{r}\frac{\partial u}{\partial r} - \frac{u^2}{r}\right), \tag{2.1}$$

where u, v, w are the components of velocity in the r, θ, z direction.

The authors [30] show that for a thin film, $h/r \ll 1$, the radial flow can be obtained from (2.1) to lowest order by solving the equations

$$-\Omega^2 r = \frac{\nu \partial^2 u}{\partial z^2},$$

where Ω is the angular velocity.

The last two formulae above used in [19] to estimate the third (z) coordinate of the waves in the case of thin film flow.

2.2 Mathematical Modeling

This section describes Dr. Sisoev derivation of the evolution equations of fluid flow [34], the numerical solutions of which are used for comparison with experimental results in Chapter 4.

2.2.1 Evolution Equations

A model given below follows from [35] with accounting non-axis-symmetric terms.

The authors, G.M. Sisoev et al., consider a film of incompressible viscous liquid, of kinematic viscosity ν and density ρ, flowing over a solid disc spinning with angular velocity Ω. A stationary cylindrical coordinate system, $(\tilde{r}, \theta, \tilde{z})$, along with the velocity field $(\tilde{u}_r, \tilde{u}_\theta, \tilde{u}_z)$, is introduced to formulate the mathematical model describing the dynamics of the film bounded by the free surface ($\tilde{z} = \tilde{h}$) and underlying solid substrate ($\tilde{z} = 0$).

The flow is governed by the continuity equation, the Navier-Stokes equations, and an appropriate set of boundary conditions: no-slip and no–penetration at the disc surface, the kinematic boundary condition, and normal stress balances at the film surface. To make these equations dimensionless, the following scaling is performed:

$$\tilde{t} = \frac{\mathrm{E}t}{\Omega}, \quad \tilde{r} = R_c e^x, \quad \tilde{z} = H_c z, \quad \tilde{u}_r = \frac{\Omega \tilde{r} u}{\mathrm{E}},$$

$$\tilde{u}_\theta = \Omega \tilde{r} \left(1 + \frac{v}{\mathrm{E}}\right), \quad \tilde{u}_z = \frac{\Omega H_c w}{\mathrm{E}}, \quad \tilde{p} = \rho \Omega^2 \tilde{r}^2 p, \quad \tilde{h} = H_c h, \tag{2.2}$$

where $\tilde{p}$ is the pressure and $\tilde{t}$ is the time. In equations (2.2), $\mathrm{E} = \nu / \left(\Omega H_c^2\right)$ represents the Eckman number; H_c and R_c are the characteristic scales for the film thickness and radial coordinate. H_c is chosen as:

$$H_c = \left(\frac{\nu Q_c}{2\pi \Omega^2 R_c^2}\right)^{\frac{1}{3}}. \tag{2.3}$$

The observed waves have a characteristic length scale which is much smaller than R_c, so the following re–scalings are introduced

$$x_\kappa = \frac{x}{\kappa}, \quad t_\kappa = \frac{t}{\kappa}, \quad w_\kappa = \kappa w, \tag{2.4}$$

where κ is a small coefficient to be determined.

In addition to the Eckman number E, the derived by Dr. Sisoev equations and boundary conditions in terms of the dimensionless variables defined in (2.2) and (2.4) incorporate two dimensionless parameterizing functions

$$\mathrm{We} = \frac{\rho\Omega^2\tilde{r}^2 H_c}{\sigma}, \quad \varepsilon = \frac{H_c}{\tilde{r}},$$

where We is the local Weber number, σ denotes surface tension, and ε is the local aspect ratio.

As shown in [35], a balance between the capillary forces and viscous stresses, which is typical for capillary waves in viscous liquid films, is provided by using

$$\kappa = \left(\frac{\sigma H_c}{\rho\Omega^2 R_c^4}\right)^{\frac{1}{3}}.$$

Analysis of experiments, also carried out in [35], revealed that a relation $\varepsilon^2/\kappa^2 \ll 1$ is satisfied in all data available when a capillary waves are observed. After omitting terms of $O\left(\varepsilon^2/\kappa^2\right)$ in the problem statement, the pressure may be eliminated and after substituting

$$u\left(x_\kappa, z, t_\kappa\right) = \frac{3q^{(u)}}{h}\left(\frac{z}{h} - \frac{z^2}{2h^2}\right),$$

$$v\left(x_\kappa, z, t_\kappa\right) = \frac{5q^{(v)}}{4h}\left(\frac{2z}{h} - \frac{z^3}{h^3} + \frac{z^4}{4h^4}\right), \tag{2.5}$$

where flow rates in radial and azimuthal directions have been introduced as

$$q^{(u)} \equiv \int_0^h u\, dz, \quad q^{(v)} \equiv \int_0^h v\, dz,$$

the approximate model follows in the form

$$\frac{\partial h}{\partial t_\kappa}+\frac{\partial q^{(u)}}{\partial x_\kappa}+\kappa\left(2q^{(u)}+\frac{\partial q^{(v)}}{\partial\vartheta}\right)=0,$$

$$\frac{\partial q^{(u)}}{\partial t_\kappa}+a_{11}\frac{\partial}{\partial x_\kappa}\left(\frac{\left(q^{(u)}\right)^2}{h}\right)+\kappa\Bigg[a_{12}\frac{\partial}{\partial\vartheta}\left(\frac{q^{(u)}q^{(v)}}{h}\right)+$$

$$a_{13}\frac{\left(q^{(u)}\right)^2}{h}+a_{14}\frac{\left(q^{(v)}\right)^2}{h}\Bigg]=\frac{\kappa}{\delta^4}\Bigg\{h+2\delta^2q^{(v)}-$$

$$b_1\frac{q^{(u)}}{h^2}+e^{-2\kappa x_\kappa}h\frac{\partial}{\partial x_\kappa}\left[e^{-2\kappa x_\kappa}\left(\frac{\partial^2h}{\partial x_\kappa^2}+\kappa^2\frac{\partial^2h}{\partial\vartheta^2}\right)\right]\Bigg\},$$

$$\frac{\partial q^{(v)}}{\partial t_\kappa}+a_{21}\frac{\partial}{\partial x_\kappa}\left(\frac{q^{(u)}q^{(v)}}{h}\right)+\kappa\Bigg[a_{22}\frac{\partial}{\partial\vartheta}\left(\frac{\left(q^{(v)}\right)^2}{h}\right)+a_{23}\frac{q^{(u)}q^{(v)}}{h}\Bigg]=$$

$$\frac{\kappa}{\delta^4}\left[\kappa he^{-4\kappa x_\kappa}\left(\frac{\partial^3h}{\partial x_\kappa^2\partial\vartheta}+\kappa^2\frac{\partial^3h}{\partial\vartheta^3}\right)-b_2\frac{q^{(v)}}{h^2}-2\delta^2q^{(u)}\right] \tag{2.6}$$

with the coefficients given by

$$a_{11}=\frac{6}{5},\quad a_{12}=\frac{17}{14},\quad a_{13}=\frac{18}{5},\quad a_{14}=-\frac{155}{126},\quad b_1=3,$$

$$a_{21}=\frac{17}{14},\quad a_{22}=\frac{155}{126},\quad a_{23}=\frac{34}{7},\quad b_2=\frac{5}{2}. \tag{2.7}$$

In 2.6, $\vartheta=\theta-\mathrm{E}t$ is the azimuthal angle related to the spinning disc. The similarity parameter

$$\delta=\left(45\kappa\mathrm{E}^2\right)^{-1}=\frac{1}{45\nu^2}\left(\frac{\rho\Omega^8R_c^4H_c^{11}}{\sigma}\right)^{\frac{1}{3}}$$

has been introduced. The film parameter δ also appears in a falling film problem [5]. E is he Eckman number and $\kappa=\left(45\delta\mathrm{E}^2\right)^{-1}$.

2.2.2 Linear Stability Analysis

With increasing radius, capillary waves are forming on a film surface. A localized version of equations (2.6) allows to compute parameters of developing linear waves. The localized equations are (see [34]):

$$\frac{\partial h}{\partial t_\kappa}+\frac{\partial q^{(u)}}{\partial x_\kappa}+\kappa\frac{\partial q^{(v)}}{\partial \vartheta}=0,$$

$$\frac{\partial q^{(u)}}{\partial t_\kappa}+a_{11}\frac{\partial}{\partial x_\kappa}\left(\frac{\left(q^{(u)}\right)^2}{h}\right)+\kappa\left[a_{12}\frac{\partial}{\partial \vartheta}\left(\frac{q^{(u)}q^{(v)}}{h}\right)+a_{13}\frac{\left(q^{(u)}\right)^2}{h}+\right.$$

$$\left.a_{14}\frac{\left(q^{(v)}\right)^2}{h}\right]=\frac{\kappa}{\delta^4}\left[h\left(\frac{\partial^3 h}{\partial x_\kappa^3}+\kappa^2\frac{\partial^3 h}{\partial x_\kappa\partial\vartheta^2}\right)-b_1\frac{q^{(u)}}{h^2}+h+2\delta^2 q^{(v)}\right],$$

$$\frac{\partial q^{(v)}}{\partial t_\kappa}+a_{21}\frac{\partial}{\partial x_\kappa}\left(\frac{q^{(u)}q^{(v)}}{h}\right)+\kappa\left[a_{22}\frac{\partial}{\partial \vartheta}\left(\frac{\left(q^{(v)}\right)^2}{h}\right)+\right.$$

$$\left.a_{23}\frac{q^{(u)}q^{(v)}}{h}\right]=\frac{\kappa}{\delta^4}\left[\kappa h\left(\frac{\partial^3 h}{\partial x_\kappa^2\partial\vartheta}+\kappa^2\frac{\partial^3 h}{\partial\vartheta^3}\right))-b_2\frac{q^{(v)}}{h^2}-2\delta^2 q^{(u)}\right], \tag{2.8}$$

The system (2.8) has the axis-symmetric stationary solution: $h=H$, $q^{(u)}=Q^{(u)}$, $q^{(v)}=Q^{(v)}$, calculated from

$$\frac{\delta^4}{H}\left[a_{13}\left(Q^{(u)}\right)^2+a_{14}\left(Q^{(v)}\right)^2\right]=H-b_1\frac{Q^{(u)}}{H^2}+\quad 2\delta^2 Q^{(v)},$$

$$a_{23}\delta^4\frac{Q^{(u)}Q^{(v)}}{H}+b_2\frac{Q^{(v)}}{H^2})+2\delta^2 Q^{(u)}=0, \tag{2.9}$$

where $Q^{(u)}=1$ in accordance with the scale (2.3).

To carry out the linear stability analysis of the basic solution (2.9), the solutions of (2.8) are represented in the following normal-mode form:

$$\left(h,q^{(u)},q^{(u)}\right)=\left(H,Q^{(u)},Q^{(v)}\right)+\left(\hat{h},\hat{q}^{(u)},\hat{q}^{(v)}\right)\exp i\left(\alpha_\kappa x_\kappa+n\vartheta_r-\omega_\kappa t_\kappa\right), \tag{2.10}$$

where the quantities with hats represent small perturbations; α_κ and n are the real wave numbers given in radial and azimuthal directions, and ω_κ is the complex wave frequency.

Substituting (2.10) into (2.8) in parallel with its linearizing leads to the following eigenvalue equation

$$i\omega_\kappa^3 + D_3\omega_\kappa^2 + D_2\omega_\kappa + D_1 = 0. \tag{2.11}$$

The dependence $\omega_\kappa\left(\alpha_\kappa, n\right)$ is found numerically determines the most growing perturbations compared with experimental data. The corresponding instant local inclination of the spiral

$$\tan\beta = \frac{1}{\tilde{r}}\frac{d\tilde{r}}{d\vartheta} = -\frac{n\kappa}{\alpha_\kappa} \tag{2.12}$$

might be compared with experimental measurements.

2.3 The Spiral Equations

Using the theory [32, 33, 45, 47], the following spiral equations were utilized:

$$a_r = r''(t) = \Omega^2 r - 8\pi f r'(t) - \frac{c}{2}\sin\beta r'^2(t),$$

$$a_s = v_s'(t) = 8\pi f(\Omega r - v_s(t)) - \frac{c}{2}\cos\beta v_s^2(t),$$

$$\tan\beta = \frac{r'(t)}{v_s(t)} = (y_x' + \frac{y}{x})/(1 - y_x' y_x) = \frac{1}{r}\frac{dr}{d\theta},$$

$$\theta'(t) = \frac{r'(t)}{r(t)}\frac{1}{\tan\beta} = \frac{v_s(t)}{r(t)}, \frac{dr}{d\theta} = \frac{r(t)r'(t)}{v_s(t)},$$

$$\frac{d^2r}{d\theta^2} = (\frac{r'^2 + r(t)r''(t)}{v_s(t)} - \frac{v_s'(t)r'(t)r(t)}{v_s^2(t)})\frac{1}{\theta'(t)},$$

$$x(t) = r(t)\cos\theta, y(t) = r(t)\sin\theta,$$

$$y_x' = \frac{r'\sin\theta + r\cos\theta\cdot\theta'}{r'\cos\theta + r\sin\theta\cdot\theta'}, \quad v(t) = (r'^2(t) + v_s^2(t))^{\frac{1}{2}},$$

$$r(0) = 0, \quad r'(0) = r_0', \quad r(T) = 200, \quad v_s(0) = 0, \tag{2.13}$$

where a_r and a_s are accelerations of fluid along radius and perpendicular to radius, f is a coefficient of fluid friction, and c is resistance of air to fluid. The formula (2.13) is not valid in vicinity of $r(0) = 0$. Therefore, we need to use another model for $\theta(t)$ on the segment $(0, b)$ for small b. Let $\theta(t) = a \cdot t$ on this segment. Then $\theta'(0) = 0$ (which was needed) and $a = \theta'(b) = \frac{r'(b)}{r(b)}\tan\beta(b)$.

It is clear that β is the angle between direction of the spiral and tangent. To find $\theta(t)$, the angle between radius at the moment t and the axes x, consider the right triangle ABC, where legs $AB = dr = r'(t)dt$ and $BC = rd\theta = r\theta'(t)$, angle β is opposite to $rd\theta$ (see Figure 2.2).

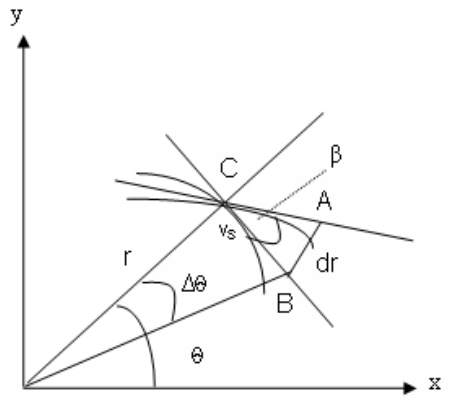

Figure 2.2 Determination of β and θ.

Note that the second and third formulae for $\tan\beta$ above can be used by image algorithms, since they do not depend on the time but only on geometric property of the spiral.

The approximate solution for this non-linear system is found using Euler's numerical method with decreasing steps of computation until approximate solutions are stabilized.

In the case of water we have $8\pi f = 0.4\ mm^{-1}$, $c = 2\ mm^{-1}$, and $r_0' = \frac{3.8\cdot 10^6}{285\cdot 2\pi\cdot 2.5\cdot 3} \approx 280$ mm/s. Here $\Omega = 40\ \frac{radian}{sec}$ is obtained from the respective graph for the reactor used, and $r'(0)$ is obtained from the experiment, in which $3.8\times 10^6\ mm^3$ is volume of a gallon of water, 285 s is the time for the water to run out of the respective capacity (see Figure 3.1), 2.5 mm is the radius of the tube, and 3 mm is the gap between the end of the tube and the disk surface.

CHAPTER 3

DATA ACQUISITION AND CAMERA CALIBRATION

3.1 Data Acquisition

The experimental set-up consists of a motor; aluminum flat/round stock; reservoir; tubing; brass adapters; bunged cords; flow-meter; copper tubing; aluminum control box; switches; return pump; miscellaneous hardware. The main characteristic of motor is given by the turntable calibration. The image of the device is shown in Figure 3.1.

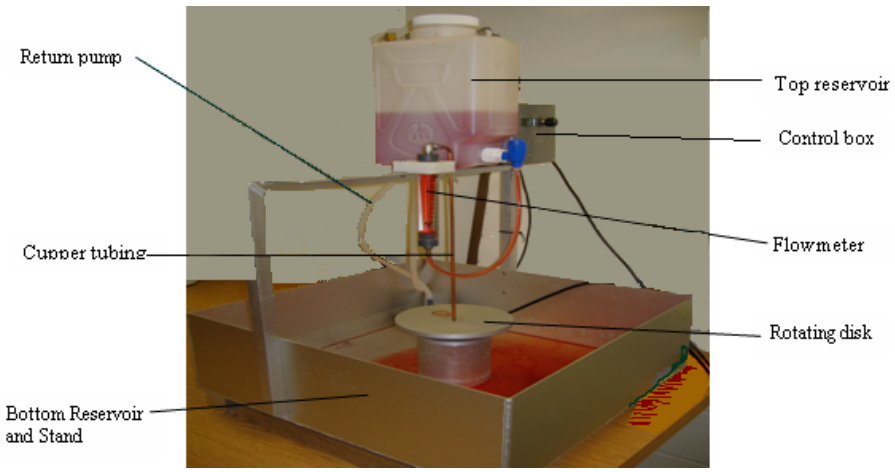

Figure 3.1 Experimental Setup.

Measurements were performed in the following way. Water contained in a plastic container with an adjustment valve for the flow was drained through copper tubing at a constant flow starting rate r_0', which can be changed in the range 0.2-0.8 lpm (liter per minute). Liquid emerged from the nozzle as a free jet pouring out onto the center of a constantly rotating aluminum disk with a diameter of 400 mm. The rotational frequency of the disk was monitored by a motor control. Water leaving the rotating disk is collected at the bottom reservoir and picked up to the top reservoir by a pump.

Ten videos were taken at different parameter settings (different arrangements of light and settings of the camera) using the portable camcorder Canon Optura 20, capable of capturing images at 30 fps (frame per second). Figure 3.2 shows a sample image of the liquid film that flows over a disk rotating with the angular velocity of 520 rpm (reverses per minute) and the flow rate 0.8 lpm. It can be seen (Figure 3.2) the film surface is covered by spiral waves.

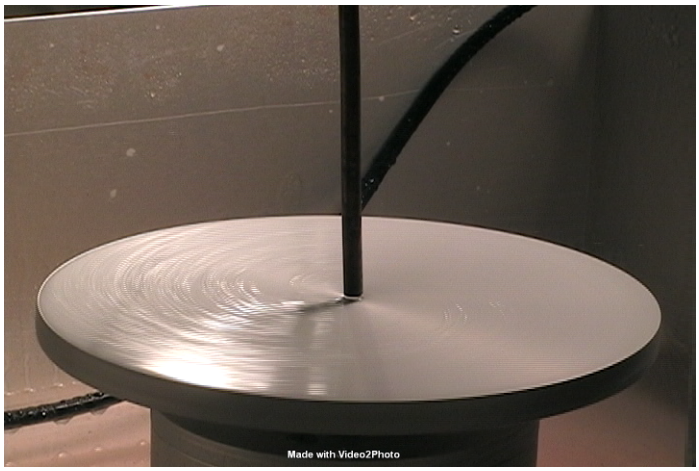

Figure 3.2 Rotating Disk Closeup.

The pattern of 8×10 squares was used to calibrate the camera (see Figure 3.3). Three

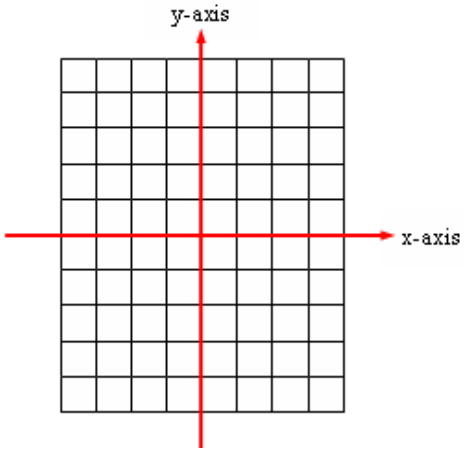

Figure 3.3 Planar Pattern.

hundred twenty points (corners of squares on the experimental pattern) were chosen in the Cartesian system coordinate with the origin in the center of the disk. Six images of the model

object were taken under different orientations by moving the model object. The technique described in [49, 51] was used for finding the intrinsic and extrinsic parameters of the camera.

3.2 Overview of Camera Calibration

Camera calibration is a necessary step in 2D and 3D computer vision in order to extract metric information from video images; and it is important for accuracy in 2D and 3D reconstruction. In particular, it is a critical task for stereovision analysis. Much work has been done, starting in the photo-gram-metric community [46], and more recently in computer vision [7, 12, 15, 18, 41, 50, 51]. Camera calibration is the process of relating the ideal model of the camera to the actual physical device and determining the position and orientation of the camera with respect to a world reference system. Depending on the model used, there are different parameters to be determined. For the pinhole camera model the parameters to be calibrated are classified in two groups:

1. Internal (or intrinsic) parameters. Internal geometric and optical characteristics of the lenses and the imaging device.

2. External (or extrinsic) parameters. Position and orientation of the camera in a world reference system.

The relationship between a 2D point (X, Y) and its image projection (x, y) is given [50, 51] by

$$\begin{bmatrix} x \\ y \\ 1 \end{bmatrix} = A \cdot [r_1, r_2, t] \cdot [X, Y, 1]^T, \quad A = \begin{bmatrix} s & \gamma & c_x \\ 0 & s & c_y \\ 0 & 0 & 1 \end{bmatrix} \tag{3.1}$$

where $[r_1, r_2, t]$ are the extrinsic parameters (the rotations and translation) that relate the world coordinate system to the camera coordinate system; A is the camera intrinsic matrix, in which (c_x, c_y) is the principal point, $s = f/s_x = f/s_y$, f is the focal length in the pixels, s is the scale factor, accuracy of which to be accounted for any uncertainty due to imperfections

in the viewing camera, $s_x = s_y$ is the effective size of the pixel, and γ is the skewness of the image axes.

3.3 Camera Calibration Accuracy

Parameters of the camera used in the experiments are: $s_x = 1/1.6 = 0.625$ mm and $s = f/s_x = 512$ mm. So, assuming that the absolute error $\triangle s$ of s is not more than half of the pixel, we have that $\triangle s/s < 0.4/512 = 0.1/128 < 0.001$.

Considering lens distortion of a camera with coefficients k_1 and k_2, the ideal (distortion-free) pixel coordinates (x, y) and the corresponding real observed or distorted image coordinates (x_d, y_d) , the relation between the coordinates of the distorted and the undistorted are:

$$x_d = x + k\,(x - c_x)\,, \quad y_d = y + k\,(y - c_y)\,,$$

$$k = k_1 r_d^2 + k_2 r_d^4, \quad r_d^2 = x_d^2 + y_d^2.$$

These relations allow us to calculate x and y, after which values X and Y are calculated from (3.1). As the results

$$\big[X, Y, 1\big]^T = \big[\, r_1, r_2, t\big]^{-1} \cdot A^{-1} \cdot [x, y, 1]^T,$$

$$x = \frac{x_d + c_x \cdot k}{1 + k}, \quad y = \frac{y_d + c_y \cdot k}{1 + k}.$$

With regard to the fact that the main error of the calibration method [12] used in our paper is determined by the effect of distortion, the standard relative deviations for x, y and X, Y are estimated, assuming for the simplicity that $c_x = c_y = \gamma = 0$. In this connection, the result in [51], page 11 is used, that the standard relative deviations for the estimates of k_1 and k_2 do not exceed 3-4%. Since in the case considered

$$x = \frac{x_d}{1 + k}, \quad y = \frac{y_d}{1 + k},$$

with regard to the main terms (assuming k is small, $k \leq 0.03$, and $k_1 = k_2$), the variations

$$dx = dx_d + x_d \cdot dk \quad dy = dy_d + y_d \cdot dk,$$

$$dk = dk_1 \cdot (r_d^2 + r_d^4), \quad \frac{dk}{k} = \frac{dk_1}{k_1} < 0.03, \tag{3.2}$$

from where,

$$\frac{dx}{x} = \frac{dx_d}{x_d} + k \cdot \frac{dk}{k}, \quad \frac{dy}{y} = \frac{dy_d}{y_d} + k \cdot \frac{dk}{k},$$

$$dr_d = dr = \frac{x \cdot dx + y \cdot dy}{(x^2 + y^2)^{1/2}}.$$

Using the fact that $\frac{dx_d}{x_d}$, $\frac{dy_d}{y_d} < \frac{0.3}{720}$, where 720 is maximal value of the number of pixels and 0.3 is the upper bound for dx_d and dy_d, it is ease to estimate that

$$\frac{dx}{x} < \frac{0.3}{720} + 0.03 \cdot 0.03 \approx 0.0013, \quad \frac{dy}{y} \approx 0.0013. \tag{3.3}$$

It follows from (3.3) that in the case $r = \sqrt{x^2 + y^2}$,

$$\frac{dr}{r} \leq \frac{dx}{x} + \frac{dy}{y} \approx 0.0026.$$

Similarly, in the case of $R = \sqrt{X^2 + Y^2}$ with regard to

$$R = \frac{1}{s}(x^2 + y^2)^{\frac{1}{2}}, \quad \frac{ds}{s} < 0.001,$$

one has

$$\frac{dR}{R} < \frac{dx}{x} + \frac{dy}{y} + \frac{ds}{s} \cdot \frac{1}{s \cdot R} \leq 0.0026 + 0.000001 < 0.003.$$

These estimates of the relative errors will be used for experimental estimation of the radial velocity component and the spiral wave inclination of the film flow as an ill-posed computational problem of differentiation [25].

CHAPTER 4

ALGORITHMS AND RESULTS

4.1 Regimes of Fluid Flow

The fluid flow over a spinning disk of 300 *rpm* and 520 *rpm* are illustrated in Figure 4.1.

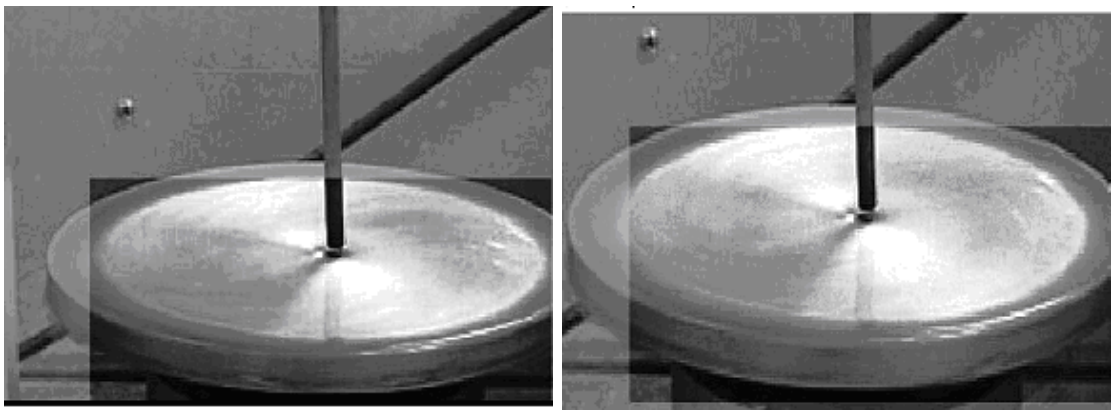

(a) (b)

Figure 4.1 Regimes of the Disk Rotation (a) 300 *rpm* and (b) 520 *rpm*.

From the observation of the fluid flows over a spinning disk follows that waves of the fluid flows create the spiral structure for different regimes. The description of the respective spirals in more details is given later.

4.2 Velocity Computation and Accuracy Estimation

The block-scheme of the velocity component estimation is given in Figure 4.2.

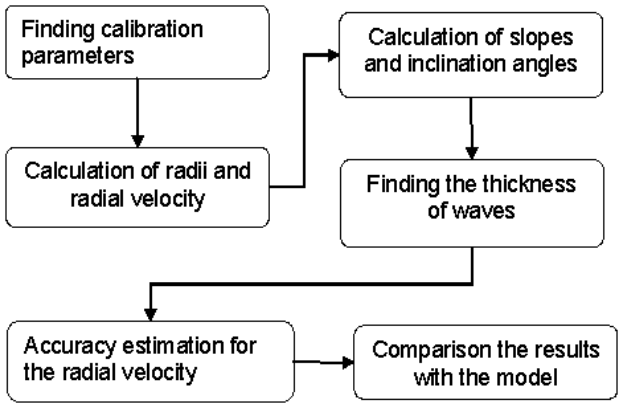

Figure 4.2 Block-Scheme of Estimation an Instantaneous Velocity.

4.2.1 Computation of Radial Velocity and Accuracy Estimation

To determine the radial velocity component, the sequences of the images of the film flows are used with the time difference equaled to $\Delta t = \mid t_2 - t_1 \mid sec.$ Choosing the system of coordinate at the center of the rotation disc, the changes of the radii at the different times are calculated: $\Delta r = \mid r_2 - r_1 \mid$, where r_1 is the value of the radius from center to the point on the wave at the moment t_1 and r_2 at the moment t_2. The estimate of the radial velocity component $r'_{exp} = \frac{\Delta r}{|t_2 - t_1|}$.

This problem is ill-posed, i.e., for such problems, arbitrary small errors of the initial data can give, in general, arbitrary large errors of the respective results. If $r(t)$ is the radius at the time t, $\tilde{R}(t)$ is its experimental value, and $\mid r(t) - \tilde{R}(t) \mid < \epsilon$ for any t, ϵ/R is the given estimate of relative error for $r(t)$, R is maximal value for $r(t)$, then

$$\Delta = |r'(t) - \frac{\tilde{R}(t+\Delta t) - \tilde{R}(t)}{\Delta t}| =$$

$$|r'(t) - \frac{r(t+\Delta t) - r(t)}{\Delta t} + \frac{r(t+\Delta t) - r(t)}{\Delta t} - \frac{\tilde{R}(t+\Delta t) - \tilde{R}(t)}{\Delta t}| =$$

$$|r'(t) - \frac{r(t+\Delta t) - r(t)}{\Delta t} + \frac{r(t+\Delta t) - \tilde{R}(t+\Delta t) + \tilde{R}(t) - r(t)}{\Delta t}| \leq$$

$$\frac{1}{2} \mid r''(t+\theta\Delta t)\Delta t \mid + |\frac{2\epsilon}{\Delta t}| \leq \frac{1}{2} M_2 \mid \Delta t \mid + \frac{2\epsilon}{\mid \Delta t \mid} = \phi(\mid \Delta t \mid), \tag{4.1}$$

where $M_2 = \max |r''(t)|$, and

$$\phi'(\mid \Delta t \mid) = \frac{1}{2}M_2 - \frac{2\epsilon}{|\Delta t|^2} = 0, \quad \mid \Delta t \mid = (\frac{4\epsilon}{R}\frac{R}{M_2})^{\frac{1}{2}},$$

$$\Delta = |r'(t) - \frac{\tilde{R}(t+\Delta t) - \tilde{R}(t)}{\Delta t}| \leq \frac{1}{2}M_2(\frac{4\epsilon}{M_2})^{\frac{1}{2}} + \frac{2\epsilon}{(\frac{4\epsilon}{M_2})^{\frac{1}{2}}} \leq 2(\epsilon \cdot M_2)^{\frac{1}{2}},$$

$$\frac{\Delta}{M_1} \leq 2(M_2 \cdot R\frac{\epsilon}{R})^{\frac{1}{2}}\frac{1}{M_1}, \quad M_1 = \max |r'(t)|. \tag{4.2}$$

The estimates in (4.1), (4.2) give the quasi-optimal value of step of differentiation Δt, for which the relative error of differentiation is given at the end of (4.2). Formulae (4.1) and (4.2) are applied for the experimental estimation of the radial velocity component and inclination angles. In our case, we can estimate $\epsilon = 1/2\ mm$, $\epsilon/R = 0.003$, due to the result of the accuracy calibration. For the proper experimental estimation of derivatives, the estimates of the maximal absolute values of the first and the second derivatives are required. That information can be obtained due to the model of spirals of the flow waves (2.13). Though that model does not regard all conditions of the film flow as the equations of Navier Stokes, it has the right relations for good estimates of the required maximal values of the first and second derivative of the motion. Indeed, the second derivative is directly proportional to the respective force due to the Newton's law as shown in equations of spiral of waves with regard to three main forces. The results of numerical solution of equations (2.13) are contained in Table 4.1.

Using this table, the value M_2 and M_1 can be estimated as: $\frac{M_2}{R} = 5063/200 = 25$, $M_1 = 781$. Therefore, using (4.2), the quasi-optimal $\Delta t \approx (0.003/25)^{\frac{1}{2}} \approx 1/100\ s$ and the respective error for estimation of the radial velocity with regarding to randomizing $\frac{\Delta}{M_1} \approx 0.065$. Thus, the relative error for estimation of radial velocity is $\approx 6.5\%$. The radii and experimental radial velocity component for one sequence of images are given in Table 4.2.

Comparison of estimated experimental velocity with the respective velocity obtained from the spiral model shows their rather closed values (see also Figure 4.3).

Table 4.1 Results of the Numerical Solutions of Spiral Equations.

$Time(s)$	$Radii(mm)$	$r'(t)$	$r''(t)$	$v_s(t)$	$v_s'(t)$	$v(t)$	$\theta(t)$	$x(t)$	$y(t)$	$\beta(radian)$
0.00	0	200	0	0	0	200	0	0	0	1.570
0.13	20	265	357	115	783	289	3.44	−6	−19	1.162
0.19	40	382	1280	177	571	422	4.59	−36	−19	1.131
0.24	60	509	2287	241	432	564	4.84	−59	−4	1.129
0.28	80	536	2504	255	404	594	4.95	−77	19	1.127
0.32	100	601	3009	287	339	665	5.20	−88	46	1.125
0.35	120	663	3516	318	276	736	5.41	−92	78	1.123
0.38	140	718	3950	345	222	797	5.59	−90	109	1.122
0.40	160	763	4313	368	177	848	5.73	−84	136	1.121
0.43	180	779	4605	391	133	871	5.85	−74	163	1.119
0.46	200	781	5063	423	237	888	5.99	−57	196	1.070

Table 4.2 Experimental Radial Velocity.

$Radii\ at\ t$	$Radii\ at\ t + \Delta t$	$Radial\ Velocity$
160	167.7	770
159	165.6	760
163	170.7	770
161	168.8	780
160	167.8	780
158	165.6	760
162	169.5	750
160	167.6	760
163	170.7	770

4.2.2 Estimation of Azimuthal Velocity Component

The azimuthal velocity component is determined by $v_{a,theor} = \frac{r'}{\tan\beta}$ (see [19]). This formula uses two values which are ill-possed to determine experimentally. The velocity $r'(t)$ was estimated above and the inclination angle β will be estimated below. Thus, using those two estimate an azimuthal velocity component can be found. For instance, if the radial velocity for the radii 160 and 167.7 is taken from Table 4.2 and the value of the inclination angle from the Table 4.4 then the azimuthal velocity $v_{a,theor} \approx \frac{r\prime}{\tan\beta} \approx \frac{770}{\tan 1.12} \approx 530\ mm/s$.

Also the film thickness h can be calculated using the following formula $h = \sqrt{\frac{2\nu r'}{R\Omega^2}}$, where ν is kinematic viscosity.

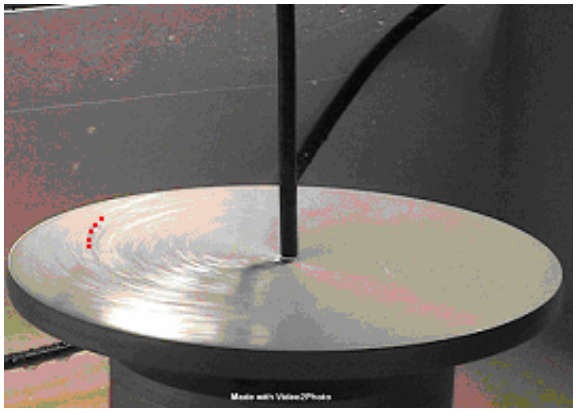

Figure 4.3 Model-Based Spiral Points (Red) on the Experimental Video Data.

4.3 Wave Front Detection

The following algorithms were developed: 1) detection of points on the waves along the same radius, 2) wavelength estimation, and 3) wave inclination estimation. The block-scheme is given below in Figure 4.4.

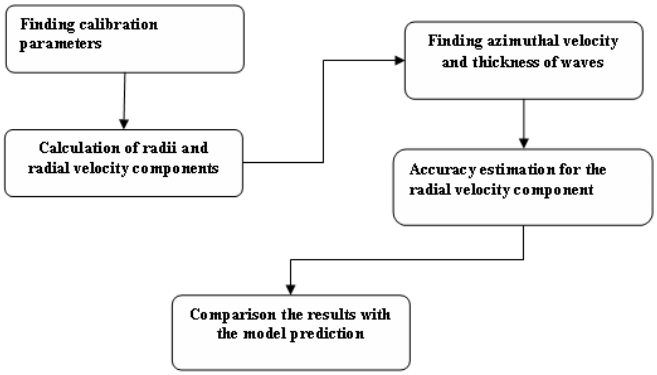

Figure 4.4 Block-Scheme of Wave Front Detection.

In order to detect the points on the waves the following sequence of operations is performed: the image scaling: the pixels with intensity $I > 220$ are increased to $I + 10$ and with $I \leq 220$ decreased to $I - 20$; the local histogram equalization; the average intensities definition for four radii at an increment $\frac{1}{57}$ radian; the fifteen first maximums finding on the averaging radius lied in the enhancement window. The image with four detected lines (a) and results of the intensity averaging of lines (b) are shown in Figure 4.3. The resulting image is shown in

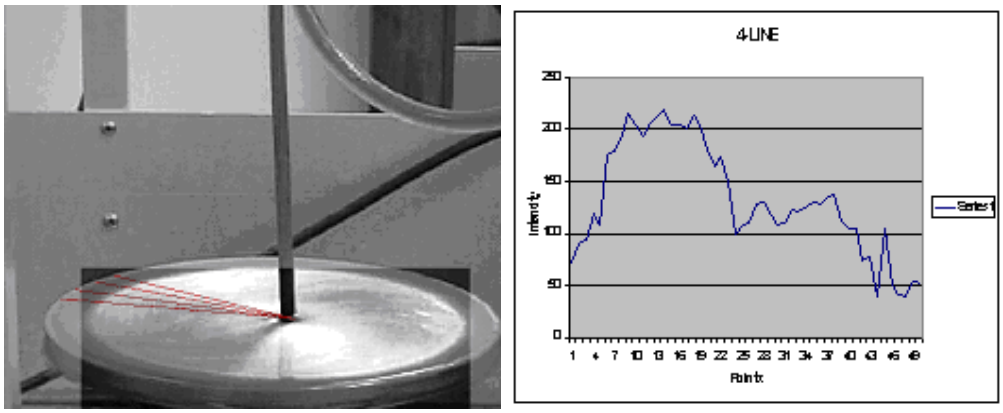

(a) (b)

Figure 4.5 (a) Enhanced Image with Selected Lines. (b) Intensity Distribution of the Average Result.

Figure 4.6.

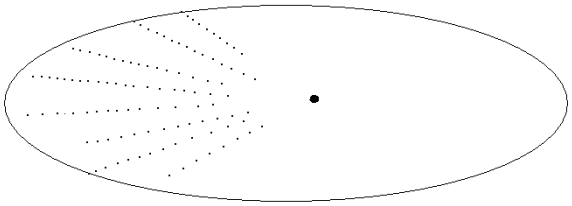

Figure 4.6 Detected Points of Waves.

4.3.1 Estimation of Inclination Angles and Wavelengths

Figure 2.2 shows the determination of an inclination angle β. The problem of estimation of β is also ill-posed [25]. So, the so-called quasi-optimal method [25] to minimize an error of estimate under the known error of initial data are used. In order to use the the radii as the function of azimuthal angle in the video images, which allows everyone to use arbitrary step along the angle, the first and second derivatives of radius over angle have to be calculated. Using formulae (2.13) and Table 4.1, the first and second derivatives are calculated for radii in the range $8 - 20\ cm$ (see Table 4.3). The quasi-optimal step $d\theta = (\frac{4\epsilon}{R}\frac{R}{M_{\theta 2}})^{\frac{1}{2}}$ is $(\approx \frac{1}{25} radian)$, where $\frac{\epsilon}{R}$ is a relative error of camera calibration (≈ 0.003) and $M_{\theta 2} = \max(\frac{d^2 r(\theta)}{d\theta^2})$ is found

Table 4.3 Calculated Results of $\frac{dr}{d\theta}$ and $\frac{d^2r}{d\theta^2}$.

$Time(s)$	$Radii(mm)$	θ'	$\frac{dr}{d\theta}$	$\frac{d^2r}{d\theta^2}$
0.00	0	0	0	0
0.13	20	5.7	46	63
0.19	40	4.5	86	186
0.24	60	4.0	126	354
0.28	80	3.2	168	514
0.32	100	2.9	209	710
0.35	120	2.7	250	922
0.38	140	2.5	291	1163
0.40	160	2.3	331	1433
0.43	180	2.1	358	1690
0.46	200	2.14	369	1695

from the Table 4.3. An error produced by image processing was estimated as $\frac{2}{M_{\theta 1}}\sqrt{M_{\theta 2}\cdot R\cdot\frac{\epsilon}{R}}$ ($\approx \pm 17\%$), where $M_{\theta 1} = \max r'(\theta) \approx 370\ \frac{mm}{rad}$. The video data of fluid flow over rotating disk of 520 rpm and the flow rate of 0.8 lpm were used to calculate the wave inclinations. The sequence of ten frames were processed to find the averaged inclination angles for radii in the range 8-20 cm. The calculated averaged inclination angles are shown in the Table 4.4. In

Table 4.4 Calculated Averaged Wave Inclinations.

The calculated inclination angles (β) (centimeter)							
R	8	10	12	14	16	18	20
β	1.32	1.19	1.12	1.00	0.99	0.97	0.93

order to calculate the radial wavelength l [37] the difference between two neighboring waves, in radial direction, was calculated: $l = r_2 - r_1$. Note that values r_1 and r_2 have to be used in the process of the averaging.

4.3.2 Correspondence to the Mathematical Model

The system (2.6) may be applied to describe axis-symmetric or spiral wave regimes if two parameters, κ^2 and (ε/κ) are small; these conditions allow one to use the boundary layer approximation. Those conditions were examined for the observed spiral waves described above. The coordinates of points on the front of curves in the radial direction were taken at a constant increment of $\pi/6$. The estimated radii are presented in Table 4.5. The parameters relevant to Table 4.5 are shown in Table 4.6, obtained by Dr. Sisoev. It can be seen from the

Table 4.5 Radii of the First and Second Waves R_1 and R_2, Respectively.

radian	cm	cm
$\pi/6$	7.994	8.304
$\pi/3$	9.899	9.928
$17\pi/36$	12.003	12.229
$21\pi/36$	13.997	14.197
$24\pi/36$	16.00	16.191
$26\pi/36$	17.893	18.063

Table 4.6 Input Data and Model Coefficients.

R_1, cm	R_2, cm	$\kappa^2 \times 10^3$	$\frac{\varepsilon^2}{\kappa^2} \times 10$	Re
7.994	8.304	7.284	0.6086	69.64
9.899	9.928	0.8604	0.5225	138.4
12.003	12.229	0.8290	0.5211	140.0
13.997	14.197	0.1765	0.4666	230.2
16.000	16.191	0.1543	0.4622	240.4
17.893	18.063	0.1002	0.4481	276.2

Table 4.6 that the principal conditions about smallness of κ^2 and (ε/κ) are fulfilled for the spiral waves as well as for axis-symmetric waves. Thus, the boundary layer approximation extended by the terms accounting for dependence on the azimuthal angle may be formulated.

To estimate inclination angle of non-axis-symmetric waves the eigenvalues ω_κ were calculated by Dr. Sisoev from Equations (2.11) for different values of radius under experimental conditions with $\Omega = 520\ rpm$ and the rate of initial fluid flow Q_c equal to 0.8 lpm. Examples of calculations are given in Figure 4.7. It is seen that non-axis-symmetric perturbations are more unstable than axis-symmetric ones. Then for a few values of radius, wave number α_κ and inclination parameter n were found in the case of maximum of amplification factors.

4.3.3 Comparison

The five videos with the sequence of ten frames for the flow rate of 0.8 lpm and the rotation of disk of 520 rpm were used for determination of the wavelengths (see Table 4.7 and Table 4.8). Average experimentally and theoretically predicted results for wavelengths are shown in Figure 4.8.

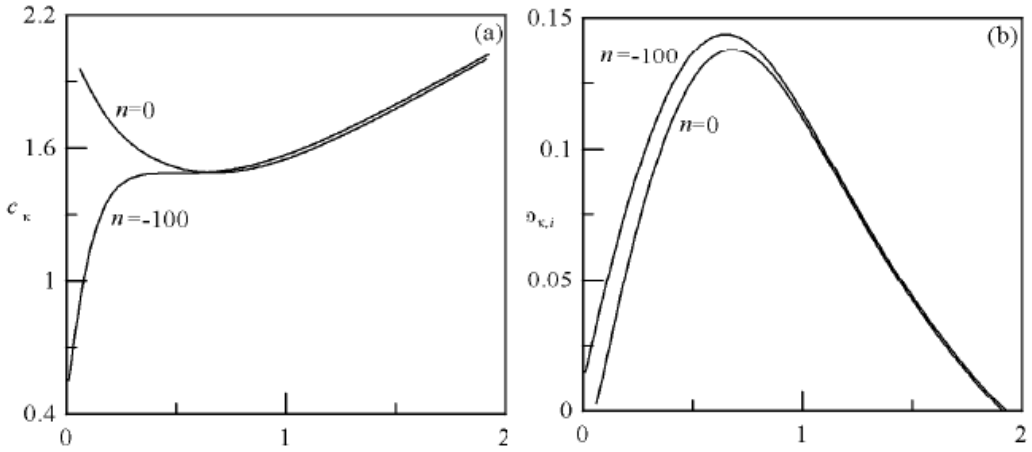

Figure 4.7 (a) Amplification Factors. (b) Axis-symmetric ($n = 0$) and Non-axis-symmetric ($n = -100$) Perturbations at $\tilde{r} = 10$ cm.

Table 4.7 Calculated Averaged Wavelengths.

Videos	The calculated wavelengths (centimeter)						
$n/radii$	8	10	12	14	16	18	20
1	.32	.30	.24	.21	.19	.18	.16
2	.33	.31	.25	.23	.21	.19	.17
3	.29	.27	.20	.18	.18	.16	.14
4	.33	.31	.22	.20	.22	.18	.16
5	.28	.26	.18	.17	.16	.14	.12

It can be seen in Figure 4.8 that there is good correspondence between theoretical prediction of wavelengths and experimental data. The average relative error is $\approx \pm 1\%$. In addition, as predicted, the wavelength decreases as radius increases.

The video data of fluid flow over rotating disk of 520 rpm and the flow rate of 0.8 lpm are used to calculate the changes of wave inclinations. The sequence of ten frames were processed to find the average change of inclination angles for radii in the range 8-20 cm. The changes of inclination angles are shown in the Table 4.9.

The experimental inclinational angle changes agree rather well with the results of the predicted inclinational angle changes. The average relative error is $\approx \pm 2\%$. In accordance with experimental observations and theoretical prediction, the inclination angle β decreases as radius grows.

Table 4.8 Calculated Averaged Wavelength Over Five Videos and Theoretically Calculated Wavelength.

Wave− length	8	10	12	14	16	18	20
Predicted	.24	.20	.18	.17	.15	.14	.13
Calculated	.31	.29	.22	.20	.19	.17	.15

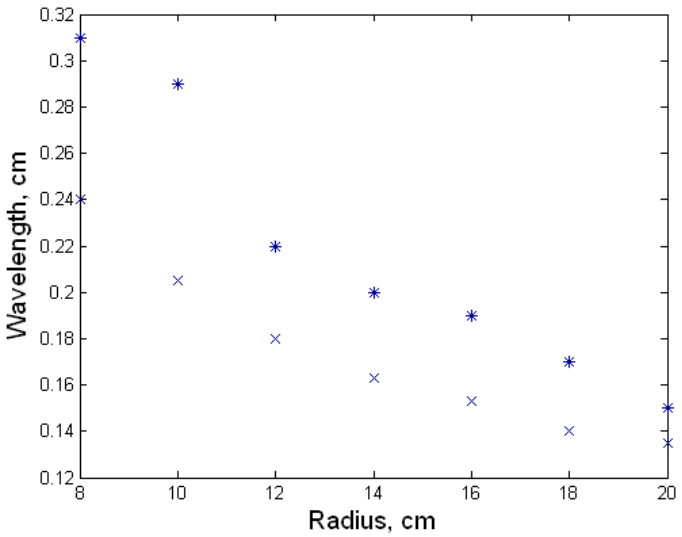

Figure 4.8 Dependence of Wavelengths Over Radii. Asterisks and x-s Correspond to Experimental and Theoretical, Respectively.

Table 4.9 Inclination Angle Changes for the Various Radii.

Wave inclination changes	8	10	12	14	16	18	20
Predicted	0	.08	.06	.04	.02	.01	.02
Calculated	0	.09	.06	.04	.03	.02	.01

CHAPTER 5

CONCLUSIONS

5.1 Summary

This thesis presents novel video-based algorithms for detection and tracking of spiral waves in a spinning disk reactor. In each frame, points on the top of multiple waves are detected and a spiral model fitted to the points. Based on these computation the wavelengths are estimated. In addition, the inclination angles between spirals and the respective circles and the radii between the center of a disk and points that lie on the front of curves in the direction of spinning disk are calculated using the so-called quasi-optimal method, which minimizes error of differentiation estimate under known error of initial data. To estimate velocity of fluid flow, we, also, use the quasi-optimal method.

Results computed from video data are compared with numbers predicted by the theoretical model. The obtained results are in good accordance with linear stability analysis of the theoretical models. In particular, the average computed wavelength is within 1% of the predicted values and a average relative error of inclination angle change computation is within 2%.

The goal of this research to develop image-based fluid flow observation algorithms capable of computing fluid flow parameters and suitable for industrial inspection applications.

5.2 Future Research

Some issues that need to be addressed in the future investigation are: (1) automated detection of points along the surface of waves of the fluid flow; (2) experiments with various physical parameters; (3) analysis of those experiments based on nonlinear solutions of the evolution system; (4) further comparing the results of the experiments with the respective models; (5) the applicability of the theory of computer vision for the evolution systems.

REFERENCES

[1] K. Aggarwal, Q. Cai, W. Liao, and B. Sabata. Nonrigid motion analysis - articulated and elastic motion (review). *Computer Vision and Image Understanding*, 70:142–156, 1998.

[2] A. Aoune and C. Ramshaw. Process intensification: heat and mass transfer characteristics of liquid films on rotating discs. *International Journal Heat Mass Transfer*, 42:2543–2556, 1999.

[3] A. Bunov, E. Demekhin, and V. Shkadov. On the nonuniqueness of nonlinear wave solutions in a viscous layer. *Appl Math Mech*, 48:691–696, 1984.

[4] A. Butuzov and I. Puhovoi. On regimes of liquid film flows over a rotating surface. *Journal of Engineering Physics*, 31(2):217–224, 1976.

[5] H. Chang and E. Demekhin. *Complex Wave Dynamics on Thin Films*. Elsevier, 2002.

[6] A. Charwat, R. Kelly, and C. Gazley. The flow and stability of thin liquid films on a rotating disk. *Fluid Mechanics*, 53(2):227–255, 1972.

[7] T. Clarke and J. Fryer. The development of camera calibration methods and models. *Photogrammetric Record*, 16(91):51–66, 1998.

[8] T. Corpetti, E. Memin, and P. Perez. Dense estimation of fluid flows. *IEEE Transactions on Pattern Analysis and Machine Intelligence*, 24:365–380, March 2002.

[9] C. Doering and J. Gibbon. *Applied Analysis of the Navier-Stokes Equation*, page 217. Cambridge University Press, 1995.

[10] L. Dorfman. Flow and heat transfer in a viscous liquid layer on a spinning disc. *Journal of Engineering Physics*, 12(3):309–316, 1967.

[11] H. Espig and R. Hoyle. Waves in a thin liquid layer on a rotating disk. *Fluid Mechanics*, 22(4):671–677, 1965.

[12] D. Forsyth and J. Ponce. *Computer Vision. A Moderm Approach*. Prentice Hall, 2003.

[13] D. Goldgof, H. Lee, and T. Huang. Motion analysis of nonrigid surfaces. In *IEEE Conference on Computer Vision and Pattern Recognition*, volume 8, pages 899–904, 1988.

[14] D. Gottlieb and S. Orszag. *Numerical Analysis of Spectral Methods: Theory and Applications*. SIAM, 1977.

[15] J. Heikkil and O. Silven. A four-step camera calibration procedure with implicit image correction. In *Proceedings of CVPR'97, IEEE*, pages 1106–1112, 1997.

[16] C. Kambhamettu, D. Goldgof, D. Terzopoulos, and T. Huang. *Computer Vision, Handbook of Pattern Recognition and Computer Vision*, volume 2, chapter 11. Academic Press, 1994.

[17] P. Kapitza and S. Kapitza. Wave flow of thin viscous liquid films. *Theor Phys*, 19:105–120, 1949.

[18] R. Klette, K. Schluns, and A. Koshan. *Computer vision. Three-dimensional data from images*. Springer, 1998.

[19] G. Leneweit, K. Roesner, and R. Koehler. Surface instabilities of thin liquid film flow on a rotating disk. *Experiments in Fluids*, 26(1-2):75–85, 1999.

[20] R. Lingwood. An experimental study of absolute instability of the rotating-disk boundary-layer flow. *Fluid Mechanics*, 314:373–405, 1996.

[21] O. Matar, G. Sisoev, and C. Lawrence. Evolution scales for wave regimes in liquid film flow over a spinning disk. *Phys. Fluids*, 16:1532–1545, 2004.

[22] S. Matsumoto, K. Saito, and Y. Takashima. The thickness of a viscous liquid film on a rotating disk. *Chem. Engng. Japan*, 6(6):503–506, 1973.

[23] S. Misra, M. Thomas, C. Kambhamettu, J. Kirby, F. Veron, and M. Brocchini. Estimation of complex air-water interfaces from particle image velocimetry images. *Experiments in Fluids*, 2006.

[24] Y. Miyasaka. On the flow of a viscous free boundary jet on a rotating disk (2nd Report. Comparison of experimental results with calculated values by means of film thickness). *Bull. JSME*, 17(113):1469–1475, 1974.

[25] V. A. Morozov. On problem differentiation and experimental information approximation algorithms. *Computational Methods and Programming*, 14:46–62, 1970.

[26] Y. Nakajima, H. Inomata, H. Nogawa, Y. Sato, S. Tamura, K. Okazaki, and S. Torii. Physics-based flow estimation of fluids. *Pattern Recognition*, 36:1203–1212, 2003.

[27] D. Needham and J. Merkin. The development of nonlinear waves on the surface of a horizontally rotating thin liquid film. *Fluid Mechanics*, 184:357–379, 1987.

[28] S. Orszag. Numerical simulation of inccompressible flows within simple boundaries. I. Galerkin (spectral) representations. *Studies in Applied Mathematics*, 50(4):293–327, 1971.

[29] O. Povarov, E. Vasilchenko, and P. Petrov. Wave flows of thin liquid layers in a centrifugal force field. *Academy of Sciences of USSR, Power Engineering and Transport*, 16(1):172–176, 1978.

[30] J. Rauscher, R. Kelly, and J. Cole. An asymptotic solution for the laminar flow of thin films on a rotating disk. *Appl. Mechanics*, 40:43–47, 1973.

[31] V. Rifert, P. Barabash, and A. Muzhilko. Stochastic analysis of wave surface structure of liquid film flowing under centrifugal forces. *High-School Bulletin, Power Engineering*, 8:62–66, 1982.

[32] J. Salen. *Fluid Flow. Handbook*. McGraw-Hill, 2002.

[33] A. A. Savelov. *Plane curves. Systematics, applications.* Nauka, 1960.

[34] G. Sisoev. Private communication. 2006.

[35] G. Sisoev, O. Matar, and C. Lawrence. Axisymmetric wave regimes in viscous liquid film flow over a spinning disk. *Fluid Mechanics*, 495:385–411, 2003.

[36] G. Sisoev, O. Matar, and C. Lawrence. Modelling of film flow over a spinning disk. *J. Chem. Technol. Biotechnol.*, 78(2-3):151–155, 2003.

[37] G. Sisoev, O. Matar, and C. Lawrence. Stabilizing effect of the Coriolis forces on a viscous liquid film flowing over a spinning disc. *Comptes Rendus Mecanique*, 332:203–207, 2004.

[38] G. Sisoev and V. Shkadov. Flow stability of a film of viscous liquid on the surface of a rotating disc. *Journal of Engineering Physics*, 52(6):671–674, 1987.

[39] G. Sisoev and V. Shkadov. Helical waves in a liquid film on a rotating disc. *Journal of Engineering Physics*, 58(4):573–577, 1990.

[40] G. Sisoev, A. Tal'drik, and V. Shkadov. Flow of a viscous liquid film on the surface of a rotating disc. *Journal of Engineering Physics*, 51(4):1171–1174, 1986.

[41] P. Sturm and S. Maybank. On plane-based camera calibration: a general algorithm, singularities, applications. In *CVPR'99*, volume 6, pages 1432–1437, 1999.

[42] S. Thomas, A. Faghri, and W. Hankey. Experimental analysis and flow visualization of a thin liquid film on a stationary and rotating disk. *Fluid Engineering*, 113(1):73–80, 1991.

[43] S. Thomas, W. Hankey, and A. Faghri. One-dimensional analysis of the hydrodynamic and thermal characteristics of thin film flows including the hydraulic jump and rotation. *ASME J. Heat Transfer*, 112(3):728–735, 1990.

[44] S. Togashi, T. Ohta, and H. Azuma. Fingering flow pattern of a liquid film on a rotating substrate. *Chem. Engng. Japan*, 34(11):1402–1406, 2001.

[45] D. Tritton. *Physical Fluid Dynamics.* Clarendon Press, 1988.

[46] R. Y. Tsai. An efficient and accurate camera calibration technique for 3D machine vision. *Proceedings of IEEE Conference on Computer Vision and Pattern Recognition*, pages 364–374, 1986.

[47] J. Walker. *Physics.* Prentice Hall, 2002.

[48] W. Woods. The hydrodynamics of thin liquid films flowing over a rotating disc. *Ph.D. thesis, University of Newcastle upon Tyne, UK*, 1995.

[49] J. Zhang, T. Huang, and R. Adrian. Extracting 3d vortices in turbulent fluid flow. *IEEE Transactions on Pattern Analysis and Machine Intelligence*, 20:193–199, 1998.

[50] Z. Zhang. Flexible camera calibration by viewing a plane from unknown orientations. In *Proceedings of ICCV'99*, 1999.

[51] Z. Zhang. A flexible new technique for camera calibration. *IEEE Transactions on Pattern Analysis and Machine Intelligence*, 22:1330–1334, 2000.

[52] L. Zhou, D. Kambhamettu, C.and Goldgof, P. K., and A. Hasler. Tracking nonrigid motion and structure from 2d satellite cloud images without correspondences. *IEEE Transactions on Pattern Analysis and Machine Intelligence*, 23:1330–1336, 2001.